Multilevel Switched-Capacitor AC–DC Step-Down Rectifier for Wireless Charging With Reduced Conduction Loss and Harmonic Content

Spencer Cochran ⬥, *Member, IEEE*, Chongwen Zhao ⬥, *Member, IEEE*,
and Daniel Costinett ⬥, *Senior Member, IEEE*

Abstract—In this article, a wireless charging architecture employing a multilevel switched-capacitor (MSC) ac–dc rectifier is investigated. The proposed MSC rectifier features a multilevel design that is scalable to accommodate different power ratings and load ranges. The topology showcases advantages for wireless power transfer (WPT) systems in terms of compactness, efficiency, impedance tunability, and harmonic attenuation. The single-stage active topology is capable of varying its low-distortion staircase input voltage to tune the WPT system for high system-wide efficiency. A seven-level, 20-W prototype is used to verify the WPT loading and loss analysis. The prototype operates at 150 kHz with up to 3:1 step-down conversion ratio to an output voltage of 5.0 V. The experimental peak dc-to-dc efficiency is 93.8% and the rectifier peak efficiency is 98.3%. The rectifier demonstrates low waveform distortion and high efficiency across many WPT loading conditions, solidifying its place as a strong candidate for wireless power applications.

Index Terms—Inverter, multilevel converter, rectifier, selective harmonic elimination (SHE), switched-capacitor converter (SCC), wireless power transfer (WPT), WPT tuning.

I. INTRODUCTION

CONSUMER mobile electronics have become prolific in daily lives. Computation capabilities, communication speeds, and display resolutions have gradually increased, resulting in power demand that approaches the daily energy limit of modern mobile battery technologies. To decrease the impact of periodic recharging, fast charging technology has been proposed and adopted by many manufacturers [1]–[3], with commercial devices supporting wired charging in excess of 20 W. Wireless power transfer (WPT) has been developed in recent years, with commercial wireless chargers integrated into many products [3].
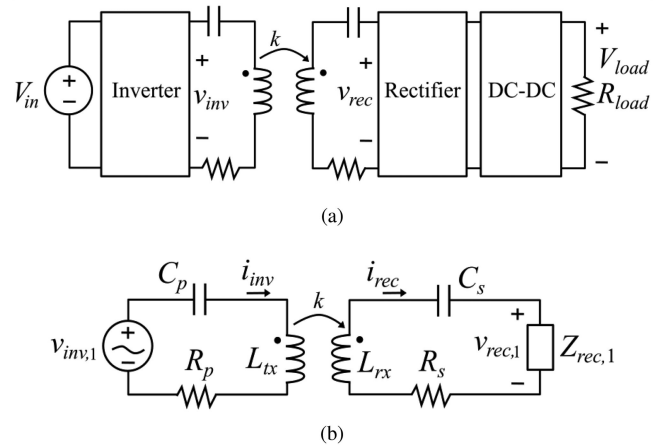
Fig. 1. (a) Block diagram. (b) Fundamental model of a typical WPT system.

A typical WPT system architecture is shown in Fig. 1(a). The tuned primary and secondary coils are referred to as the WPT tank. The inverter presents an ac voltage to the WPT tank, inducing a voltage on the receiver side. The secondary-side waveform is then rectified back to dc, and the dc–dc converter steps the voltage up or down to regulate the output V_{load}. Motivated by the bandpass nature of the WPT coil tuning, the first harmonic approximation (FHA) is used to model the system as in Fig. 1(b). In this work, v_{inv} and v_{rec} refer to the ac (plus harmonics) inverter and rectifier voltages, respectively. Variables $v_{\text{inv},1}$ and $v_{\text{rec},1}$ are the fundamental components of these voltages.

Fig. 1 illustrates two important system characteristics: distortion and loading. The FHA model assumes that negligible power transmission and loss occur at any harmonic other than the fundamental. Furthermore, even with broadband modeling, the presence of additional harmonic components increases the risk of interference with other electronics and may necessitate additional filtering components [4], [5] and increases loss due to reduced efficiency of power transfer at harmonic frequencies. Thus, solutions whose real waveforms are well-approximated by the FHA are advantageous. Second, the complex rectifier impedance Z_{rec} loads the system. Therefore, the fundamental impedance component $Z_{\text{rec},1}$ is directly responsible for system-wide efficiency [1]. An optimal value of $Z_{\text{rec},1}$ ensures the highest system-wide efficiency [6]. These metrics

of total harmonic distortion (THD) and real-time impedance tuning (ability to vary $Z_{\text{rec},1}$) are used to evaluate WPT rectifiers.

Two other metrics are especially important for small consumer devices: efficiency and size. A high efficiency circuit is always desired, but it is especially important for thin handheld electronics that must remain cool to the touch. Also, size is a premium in tightly packed consumer device circuit boards; so low-footprint-area topologies using low-profile components are desired. Avoiding bulky and lossy dc filter inductors [7], [8] and topologically combining stages (integrating the rectifier and dc–dc converter) are attractive attributes for WPT rectifiers.

The diode full bridge (DFB) of half bridge (DHB) rectifier (without a dc–dc conversion stage) is attractive for its simplicity and compactness. However, the rectifier input impedance is fixed as a function of R_{load} under the FHA approximation [1]. Furthermore, the square wave voltage produced by the DFB is known to contain high harmonic content. These shortcomings result in high-distortion waveforms and nonoptimal values of $Z_{\text{rec},1}$ that can cause large tank currents [9]. Because of the static value of $Z_{\text{rec},1}$, the work in [9] requires V_{in} be tuned in order to keep V_{load} constant across different values of R_{load}.

Another popular approach is including a dc–dc converter between the DFB and V_{load}. This may be implemented with a buck [10], boost [11], cascade buck and boost [12], or buck–boost [6], [13], [14]. For any of these approaches, impedance $Z_{\text{rec},1}$ is now a function of both R_{load} and dc–dc converter duty cycle D. Depending on the dc–dc converter, impedance magnitude $|Z_{\text{rec},1}|$ can now be increased, decreased, or both relative to the case without a dc–dc converter [6]. The drawback is that these implementations not only add a second stage to the rectification scheme but also the second stage requires a large filter inductor. The bulky dc filter inductor can be avoided by using a dc–dc switched-capacitor converter (SCC) [15], [16] in lieu of buck/boost implementations. However, discrete steps in regulation (and consequently $|Z_{\text{rec},1}|$) make this implementation challenging [17].

Replacing the DFB devices with transistors, a synchronous full bridge (Sync FB) can reduce conduction losses due to diode forward voltage without significantly altering in-circuit behavior [18]–[21]. If the transistor full bridge is additionally controlled through phase or duty-cycle modulation, it is considered an active full bridge (AFB). An AFB can control $\angle Z_{\text{rec},1}$ by varying the switching times within the period [22]. The ability to vary $\angle Z_{\text{rec},1}$ equips the rectifier to inject reactance into the circuit to retune the system in the event L_{rx} and C_s do not resonate at the fundamental frequency [23]. With the combination of an AFB and an up/down regulator (such as a Sync FB + LDO [24]), the rectifier could theoretically reach any value of $Z_{\text{rec},1}$, enabling WPT tank retuning for optimal system-wide efficiency over a wide range of coil mismatch, coupling change, output power, and interference situations.

However, each of the reviewed approaches has some set of drawbacks. The DFB is compact and single-stage, but it cannot retune its impedance or address waveform distortion. Multistage approaches enable control of $|Z_{\text{rec},1}|$, but those with buck/boost style dc–dc converters require a large filter inductance [12]–[14].

SCC converters avoid the filter inductor, but they produce discrete steps in $|Z_{\text{rec},1}|$, making precise impedance tuning more difficult. AFB rectification enables reactance injection, but even in the case of three-level modulation, their waveforms produce significant harmonic content, and they require an additional dc–dc for bidirection impedance magnitude conversion. More-complex resonant resonant class-E rectifiers [5] can exhibit very low distortion but are difficult to design over a wide range of operating conditions.

Switched-capacitor step-down rectifiers have previously been studied for ac–dc rectification [25] in wired applications where THD, impedance control, and compactness were of lesser concern. In this article, the multilevel switched capacitor (MSC) rectifier is proposed as a holistic solution for WPT applications which simultaneously addresses each evaluation metric by achieving low-THD, regulated impedance, small size, and high efficiency. In order to achieve these metrics, the topology, design, and modulation are tailored to the intended application. The single-stage topology requires no dc filter inductor, can inject reactance ($\angle Z_{\text{rec},1}$), possesses both up and down regulations of $|Z_{\text{rec},1}|$, is highly efficient, and significantly reduces WPT tank distortion (relative to the nominal square wave case) via its staircase waveforms.

The rest of this article is organized as follows. Section II further motivates the impedance tuning characteristics of the MSC topology. Section III establishes the main operating principle of the MSC WPT system, and Section IV investigates how the MSC modulation scheme interacts with the FHA model. Section V derives loss mechanisms, and Section VI supports the analysis with experimental testing. Finally, Section VII concludes this article.

II. TOPOLOGY COMPARISON

To emphasize the impedance and tunability differences among the reviewed topologies, an example application is examined under the FHA. An example tank is employed for comparing different rectification approaches in Fig. 2. These example tank parameters are set such that $L_{tx} = L_{rx} = 10\,\mu\text{H}$, the $L_{rx}|C_s$ pair resonates at 150 kHz, and $R_p = R_s = 100\,\text{m}\Omega$. These coil inductances and quality factors are within a realistic range: A market-available $10\,\mu$H WPT coil has equivalent series resistance (ESR) values between 43 and 554 mΩ through the first five harmonics [26]. In this example, the consumer device is paired with a transmitter system that is tuned to 100 kHz, that is, $|Z_{Ltx}| = |Z_{Cp}|$ at 100 kHz.

Each of the cases in Fig. 2 shows the tank efficiency (color), power contours (black lines), peak efficiency point (black X), and peak 20-W efficiency point (black O). Furthermore, the DFB, DFB and buck converter (DFB + buck), and AFB topologies are included. These are denoted by the black dot, dashed line, and translucent white area, respectively. Each topology is overlaid onto the plots such that the output voltage remains constant at $V_{\text{load}} = 5$ V. The AFB and buck converter (AFB + buck) topology is not pictured as it can reach any point on Fig. 2 via full control of $Z_{\text{rec},1}$.
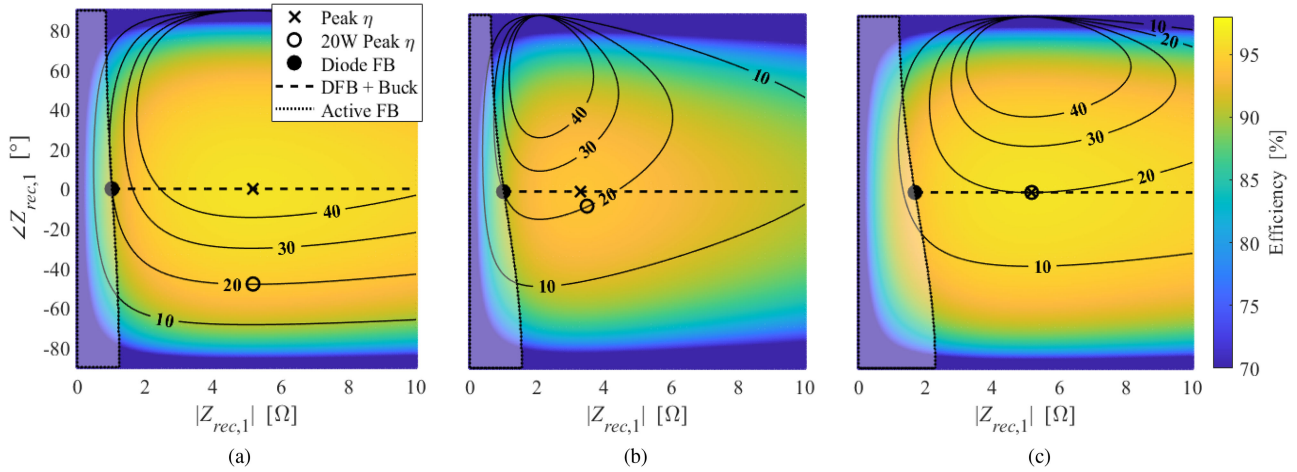
Fig. 2. Efficiency (color) and power (contours) plots with rectification strategies and optimal points overlaid. $V_{\text{load}} = 5$ V for all cases. The cases have (a) $k = 0.55$ and $V_{\text{in}} = 26.2$ V, (b) $k = 0.35$ and $V_{\text{in}} = 18.7$ V, and (c) $k = 0.55$ and $V_{\text{in}} = 16.4$ V.

The first case in Fig. 2(a) shows the system with a nominal coupling value of $k = 0.55$. Here, inverter voltage V_{in} is set to 26.2 V so that the diode full bride rectifier experiences $P_{\text{out}} = 20$ W, the desired system power. Because the DFB cannot vary its input impedance, maintaining $P_{\text{out}} = 20$ W means that a coupling change to $k = 0.35$ forces an input voltage change to $V_{\text{in}} = 18.7$ V in Fig. 2(b).

Taken in isolation, Fig. 2(a) and (b) illustrates some important points. First, the AFB topology does no better in either scenario: The duty cycle impedance step-down mechanic is not helpful for these cases. Second, the DFB + buck topology is beneficial to improve the efficiency of 20-W power transfer in Fig. 2(b). Here, the step-up impedance transformation is useful because $Z_{\text{rec},1} = 1.0\,\Omega$ and $Z_{\text{rec},1} = 4.3\,\Omega$ both yield 20 W, but the latter does so at a higher efficiency by reducing WPT tank current. Finally, full impedance control (as with the AFB + buck) is beneficial in both cases. Reaching the 20-W peak efficiency point requires full control of $Z_{\text{rec},1}$, and it showcases $\approx 4\%$ higher efficiency than the DFB in both cases. For Fig. 2(a) and (b), the DFB efficiencies are 90.7% and 90%, compared with the optimal 20-W load efficiencies of 94.5% and 94.1%, respectively.

Fig. 2(c) extends the concept of leveraging V_{in} to the case with full impedance control. This optimal case revisits $k = 0.55$ but sets $V_{\text{in}} = 16.4$ V so that the overall most efficient operating point occurs at 20 W. Because the $L_{rx}|C_s$ pair is tuned to the operating frequency (150 kHz), this point occurs at $\angle Z_{\text{rec},1} = 0$. Here, the DFB + buck and AFB + buck can both reach the optimal point: 20-W output at 96.2%.

Therefore, cases with nonoptimal transmitter characteristics [like Fig. 2(a) and (b)] benefit from both magnitude and reactance tuning. Cases where communication enables primary-side optimization [like Fig. 2(c)] benefit from magnitude tuning. The MSC topology is able to fully control $Z_{\text{rec},1}$, hitting each of the optimal 20-W operating points in Fig. 2. Additionally, the topology has reduced THD, avoids bulky filter inductors, and combines the rectification and dc–dc conversion stages, making it a promising candidate for miniaturization in mobile electronics applications.
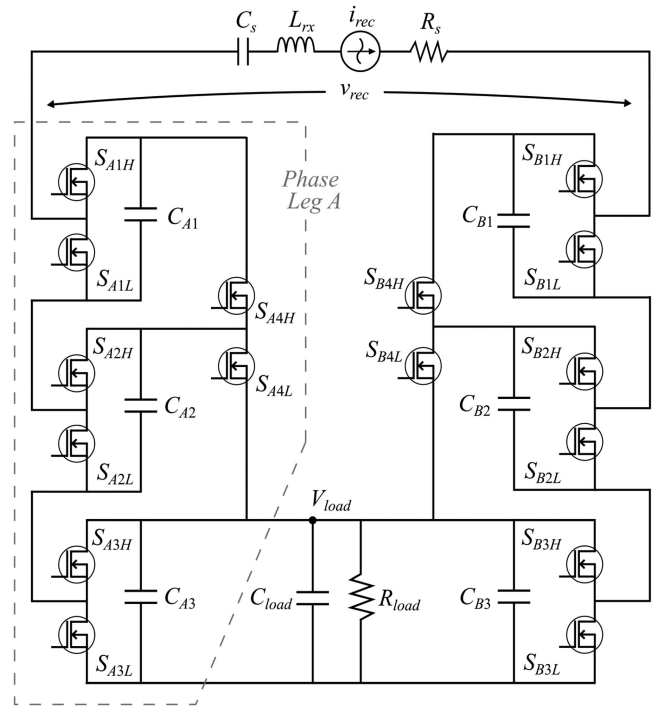

Fig. 3. Schematic circuit of the proposed seven-level switched-capacitor ac–dc rectifier with 3:1 voltage step-down.

III. MULTILEVEL SWITCHED CAPACITOR

The schematic circuit of the MSC rectifier is shown in Fig. 3, using a seven-level implementation as an example. The topology comprises a bipolar series–parallel SCC. Because the topology is modular, it can be expanded to more levels. The seven-level implementation is selected in this article to achieve conversion ratios of above 3:1, which mimics the buck converter's impedance transformation capability as highlighted in the previous section. In accordance with the fundamental model, elements L_{rx}, C_s,
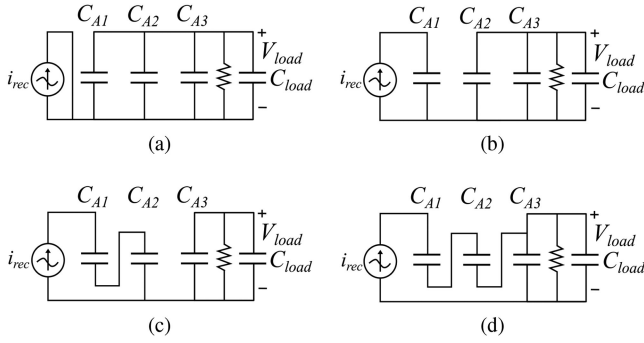
Fig. 4. Operation principle of step-down MSC rectifier in one half-cycle. Operation sequence: 1-2-3-4-3-2-1. (a) Subinterval 1. (b) Subinterval 2. (c) Subinterval 3. (d) Subinterval 4.
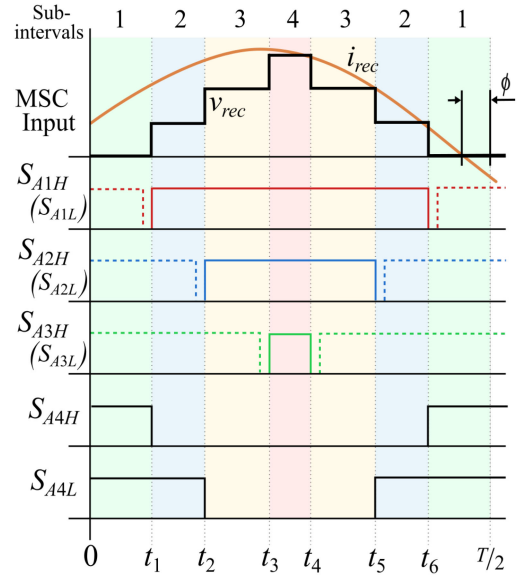

Fig. 5. Control signal sequence for 7-level SC rectifier in one input half-period. For each gate signal, Solid line: high side switches and charge sharing switches (S_{A1H}, S_{A2H}, S_{A3H}, S_{A4H}, S_{A4L}); dashed line: low side switches (S_{A1L}, S_{A2L}, S_{A3L}).

and R_s are included, while sinusoidal current i_{rec} is used as the source for the rectifier model.

The topology of Fig. 3 forms a single-phase rectifier with two identical legs, $Phase\ Leg\ A$ and $Phase\ Leg\ B$ (not labeled in Fig. 3), operated symmetrically with $180°$ phase shift synchronized to the zero-crossings of v_{rec}. The circuit composition and control signal sequence of the two legs are the same; so only the positive half-cycle of v_{rec} is discussed in detail. All devices in the rectifier switch ON and OFF once per period, and switching devices in a half-bridge configuration, such as S_{A1H} and S_{A1L}, have complementary schemes.

This topology is previously studied as a wired ac–dc rectifier in [25]; however, switching actions of all devices in one phase leg were synchronized such that the differential voltage v_{rec} was a two-level square wave with a fixed conversion ratio. In this work, individual switch pairs in a phase leg are independently controlled to generate a multilevel staircase waveform, instead of a two-level square wave. Therefore, the low-order harmonic magnitudes are smaller than those in a square wave of the same fundamental amplitude. Additionally, the modulation pattern is varied to allow variable conversion ratio and variable phase alignment. Together, these two modulation freedoms allow the MSC to vary both the magnitude ($|Z_{rec}|$) and angle ($\angle Z_{rec}$) of the impedance presented to the WPT system, which can be used to optimize system efficiency as discussed in Section I.

Equivalent circuits of the proposed seven-level SC rectifier during switching subintervals in one half-cycle are shown in Fig. 4. The MSC switching pattern is quarter-wave symmetric with seven subintervals per input half-cycle. The operation sequence in one half-cycle is subintervals

$$1 \rightarrow 2 \rightarrow 3 \rightarrow 4 \rightarrow 3 \rightarrow 2 \rightarrow 1$$

and the control signals for switching devices in $Phase\ Leg\ A$ are given in Fig. 5.

In order to simplify analysis, two assumptions are made about the converter design: 1) All flying capacitors are large enough to ensure small voltage ripple, and the output capacitance C_{load} is sufficient to ensure a constant V_{load}; 2) all subinterval durations are much longer than the switched capacitor circuit internal RC dynamics so that the slow switching limit (SSL) applies at given switching frequency (150 kHz) [27]. Under these

assumptions, the flying capacitor voltages are approximately dc, with magnitude equal to the load voltage V_{load}.

In subinterval 1, the input voltage of the rectifier is 0 V, and all low-side switches (S_{xxL}) conduct to provide a return path for the input current. All flying capacitors, $C_{A1} - C_{A3}$, are connected in parallel with the output, discharging to the load, as shown in Fig. 4(a). In subinterval 2, C_{A1} is charged by the input current, and the input voltage is equal to the load voltage V_{load}. By switching additional flying capacitors in series with the input, the rectifier can generate an input of $2V_{load}$ in Fig. 4(c) or $3V_{load}$ in Fig. 4(d).

Because the bottom module is directly shorted to the output capacitor, the voltage of C_{A3} is always the output voltage V_{load}. As such, C_{A3} (and C_{B3}) can be combined with C_{load} and implemented as a single component. Flying capacitors C_{A1} and C_{A2} are periodically shorted to the output by S_{A4H} and S_{A4L}, respectively, at the instances t_5 and t_6, as shown in Fig. 5. For the opposite half-cycle, $Phase\ Leg\ A$ stays in subinterval 1 where all flying capacitors are clamped to the output dc bus, while the $Phase\ Leg\ B$ operates in the same manner with $180°$ phase shift to provide the negative half-cycle of v_{rec}. In a full period, this MSC rectifier generates a seven-level staircase voltage v_{rec} at the input terminal, with the peak value $|v_{rec}(t)| = 3V_{load}$.

For the seven-level SC topology, the number of capacitors in one phase leg is $n_m = 3$. By stacking more modules ($n_m > 3$), the MSC can achieve a higher voltage step-down ratio, directly affecting the converter's input impedance. However, more switching devices and flying capacitors are required, which may contribute to higher conduction and switching loss as well as increased size. Therefore, it is necessary to understand how the number of modulation levels affects both the rectifier's impedance characteristics and the rectifier's conversion efficiency.

IV. MSC FUNDAMENTAL REPRESENTATION

The fundamental model of Fig. 1(b) is again referenced. The rectifier fundamental voltage and the dc load voltage are divided to define modulation index [1]

$$M = \frac{|v_{\text{rec},1}|}{V_{\text{load}}} \quad (1)$$

a metric used to describe the total step-down effect of the rectification stage. In general, the output voltage (V_{load}) is determined by the combination of modulation index M, rectifier switching times (i.e., $\angle Z_{\text{rec},1}$), and R_{load}. By design, this steady-state modeling work sets $V_{\text{load}} = 5$ V, but a final design would utilize closed-loop control for regulation. The proposed MSC rectifier relies on modulation index to achieve rectifier impedance magnitude transformation. The modulation of multilevel converters has been studied extensively, where either carrier-based modulation [28], [29] or selective harmonic elimination (SHE) [30] is employed.

The equivalent impedance of the MSC rectifier when the rectifier voltage and current are in phase is

$$Z_{\text{rec},1} = |Z_{\text{rec},1}| = \frac{M^2}{2} R_{\text{load}}. \text{ [1]} \quad (2)$$

Here, $Z_{\text{rec},1}$ is a simple function of the modulation index and the load. However, because the circuit is actively switched, the rectifier input voltage and input current can be set out of phase by changing the device switching times. In the case of a nonzero phase shift ($\angle Z_{\text{rec},1} = \phi \neq 0$), the total fundamental impedance of the MSC rectifier is given by

$$Z_{\text{rec},1} = \frac{M^2}{2} R_{\text{load}} \cdot \cos(\phi) e^{j\phi}. \quad (3)$$

For a seven-level SC rectifier, both the modulation index and switching time determine the total input impedance at a given load. The upper and lower bounds of M depend on the number of levels in the converter and the specific modulation scheme selected. With $n_m = 3$, M can range from 0 to $n_m \cdot 4/\pi = 3.81$ using carrier-based modulation. In the extreme, when $M = 3.81$, the seven-level staircase waveforms resemble a two-level square wave which provides a maximum rectifier impedance. Although the fundamental amplitude changes with modulation index, the instantaneous peak voltage remains $|v_{\text{rec}}(t)| = 3V_{\text{load}}$ as long as each modulation level is employed.

Motivated in Section II, Fig. 6 compares the functional operating area using the example in Fig. 2(c). The operating range of the seven-level circuit is shown by the colored portion of Fig. 6 and covers most of the graph area. Again, the levels of the contour plot in Fig. 6 show output power. The empty white section near the top right of Fig. 6 represents the area where the modulation index must exceed $M = 3.81$ for a given output voltage of $V_{\text{load}} = 5$ V, and the MSC cannot, therefore, operate in this region as designed with $n_m = 3$.

To extend impedance transformation ability, more modules can be stacked to allow a larger number of voltage levels, which essentially increase the range of M from modulation perspective. In general, the achievable modulation range is $0 <$
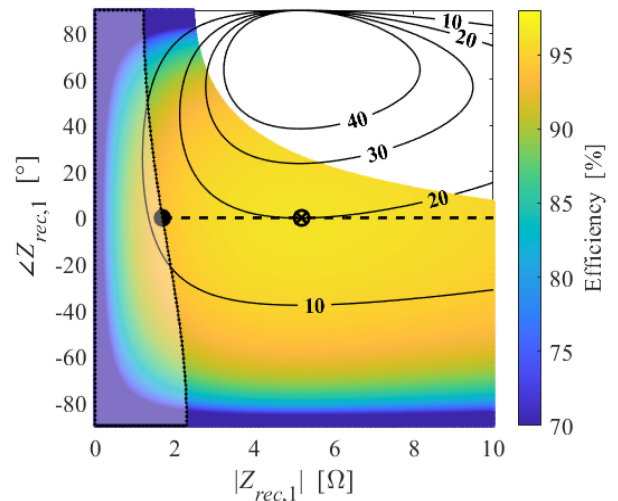

Fig. 6. Operation region of the MSC under the $k = 0.55$ and $V_{in} = 16.4$ V example of Section I. The MSC cannot reach the white region because $M > 3.81$. The most efficient 20 W operating point for this example tank is $\eta = 96.2\%$.
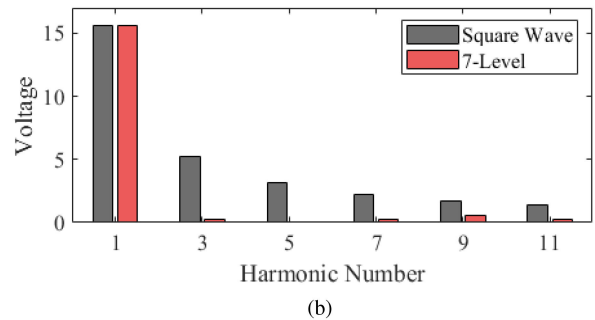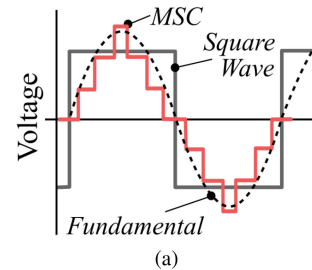

Fig. 7. Comparison of the seven-level SC rectifier input voltage and a square wave voltage with the same fundamental component. (a) Time domain waveforms. (b) Spectrum comparison.

$M < n_m \cdot 4/\pi$. This scalability helps to accommodate different applications by adding/subtracting modules.

The seven-level SC rectifier modulation reduces the harmonic content in the WPT circuit. Compared with a full-bridge rectifier, the multilevel converter generates low THD, near-sinusoidal voltages with a switching frequency equal to the fundamental frequency [29]. In Fig. 7(b), the harmonics of a sinusoidally modulated seven-level staircase waveform are compared with a two-level square waveform with the same fundamental magnitude. The MSC waveform shows significantly lower third, fifth, and seventh harmonics. This reduces the necessary size (and

loss) of filtering, and it facilitates compliance with bandwidth requirements and electromagnetic interference (EMI) standards. If necessary, the harmonics of the MSC can be further reduced by employing SHE to nullify a range of low-order harmonics such as the third and fifth with a programmed switching pattern [30].

Overall, the MSC topology enables lower waveform distortion, provides complete impedance tunability, and avoids bulky filter inductors, resulting in a higher system-wide efficiency and increased secondary-side compactness. Next, the loss mechanisms of the converter are analyzed to develop a design that enables these benefits.

V. Loss Analysis

This section analyzes several major losses of the proposed MSC rectifier. The following loss analysis is based on the control sequence shown in Fig. 5 and assumes that all switching devices are identical.

1) Conduction Loss: The conduction loss consists of two parts: the conduction loss due to the $R_{\rm dson}$ of the switching devices in a current path; the conduction loss induced by the flying capacitor ESRs. The total conduction loss is

$$P_{\rm cond} = 2 \cdot n_m \cdot I_{\rm rms}^2 \cdot R_{\rm ds(on)} + P_{\rm ESR,C} \tag{4}$$

where $I_{\rm rms}$ is the rms value of the input current $i_{\rm rec}$, and $P_{\rm ESR,C}$ is the conduction loss of the flying capacitors. The function for calculating $P_{\rm ESR,C}$ is

$$P_{\rm ESR,C} = \sum_{x=1}^{n_m} I_{\rm recRMS}(x)^2 \cdot R_{\rm ESR,C} \tag{5}$$

where the function $I_{\rm recRMS}$ describes the rms equivalent on current seen by the capacitor (not including charge redistribution current) in modulation level $x = \{1, 2, 3\}$. Equation (6) defines $I_{\rm recRMS}$ with $(t_{7-x} - t_x)$ as the ON-time of level x ($x = 1$ denotes $v_{\rm rec} = 1 \cdot V_{\rm load}$, $x = 2$ denotes $v_{\rm rec} = 2 \cdot V_{\rm load}$, etc.) and $R_{\rm ESR,C}$ as the series resistance of each flying capacitor. Under the FHA, (6) assumes $i_{\rm rec}$ is a single-frequency sinusoid

$$I_{\rm recRMS}(x) = \frac{1}{2} |i_{\rm rec}|^2 f_s (t_{7-x} - t_x) \cdot$$

$$\left(2 + \frac{\sin(2(\omega t_x - \phi)) - \sin(2(\omega t_{7-x} - \phi))}{\omega(t_{x-7} - t_x)} \right) \cdot \tag{6}$$

A. Switching Loss

Each level change in $v_{\rm rec}$ is consequent of one pair of half-bridge switching actions. Generalizing this action with Fig. 8, the dead time waveforms are approximated as linear, under the assumption that the dead time is very short relative to circuit dynamics and the fundamental operating period. One of four scenarios occurs. A threshold current is defined as

$$I_{\rm th} = 2C_{\rm oss} \frac{V_{\rm load}}{t_d} \tag{7}$$

where t_d is the dead time. Current $I_{\rm lc}$ is the approximated-constant current during the dead time, defined by the value of $i_{\rm rec}$ at the switching instant. The relationship between $I_{\rm lc}$ and
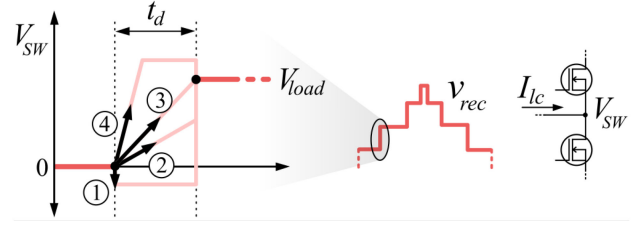

Fig. 8. Linearized dead time for a rising edge showing the potential $V_{\rm sw}$ translation cases dependent on $I_{\rm lc}$.

TABLE I
HIGH AND LOW SIDE SWITCH LOSS CONTRIBUTIONS FROM FIG. 8

		Loss Mechanism			
Case		ON	OFF	Diode	C_{oss}
1:	$I_{lc} < 0$	HS	LS	LS	HS
2:	$I_{lc} < I_{th}$	HS	LS	—	HS
3:	$I_{lc} = I_{th}$	—	LS	—	—
4:	$I_{lc} > I_{th}$	—	LS	HS	—

$I_{\rm th}$ determines the case as shown in Table I. A negative current (case 1) forces diode conduction, a small current (case 2) reduces hard switching loss, exact zero-voltage switching (ZVS) current (case 3) only results in $T_{\rm off}$ loss, and a large dead time current (case 4) causes overcharging of the switch node.

The switching loss mechanisms are summarized by

$$P_{\rm on} = {1}/{2} |I_{\rm lc}| V_{\rm on} t_{\rm on} f_s \tag{8}$$

$$P_{\rm off} = {1}/{2} |I_{\rm lc}| V_{\rm load} t_{\rm off} f_s \tag{9}$$

$$P_{\rm diode} = V_d |I_{\rm lc}| t_{\rm dc} f_s \tag{10}$$

$$P_{\rm coss} = {1}/{2} C_{\rm oss} V_{\rm on}^2 \tag{11}$$

where parameters $V_{\rm on}$ and $t_{\rm dc}$ are defined as

$$V_{\rm on} = V_{\rm load} (I_{\rm th} - I_{\rm lc})/I_{\rm lc} \tag{12}$$

$$t_{\rm dc} = t_d (I_{\rm lc} - I_{\rm th})/I_{\rm th} \tag{13}$$

for cases 2 and 4, assuming linearized dead time waveforms during the short dead time, as shown in Fig. 8. These parameters are $t_{\rm dc} = t_d$ and $V_{\rm on} = V_{\rm load} + V_d$ for case 1. Parameters V_d, $t_{\rm on}$, and $t_{\rm off}$ are the body diode voltage, turn-ON time, and turn-OFF time, respectively. Since all devices switch ON and OFF only once in a full period, the switching frequency f_s is the WPT carrier frequency. Gate loss is not considered in the power stage model. Fig. 8 and Table I present the loss breakdown for rising edges, but the same approach is applied to falling edges and inverter switching actions (with appropriately modified equations and thresholds).

B. Charge Sharing Loss

In the MSC converter, each flying capacitor C_{xi} is charged by $i_{\rm rec}$ during the portion of the period where that capacitor contributes to $v_{\rm rec}$, resulting in a small increase in capacitor
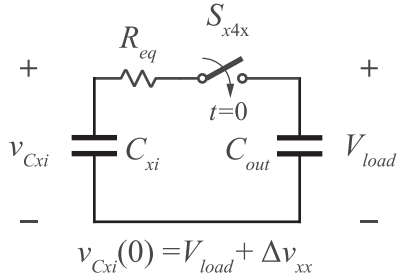
Fig. 9. Charge sharing loss equivalent circuits in MSC rectifier: capacitor to capacitor.

Fig. 10. Experimental setup showing the FPGA controller, inverter, tuned WPT tank, and rectifier.

voltage Δv_{xx}. During the nonactive half period, charge sharing switches S_{x4x} turn ON for $T_s/2$ and the respective flying capacitors are connected in parallel with the output capacitance C_{out}. This causes a pulsed current which equalizes the capacitor voltages through a resistive path, resulting in charging sharing loss [27]. It is assumed that $C_{\mathrm{out}} \gg C_{xi}$, either by design or due to the connection of multiple flying capacitors in parallel with the output at any moment, and, therefore, V_{load} remains nearly constant during the process. Charge sharing loss is modeled using the generalized equivalent charge sharing circuit of Fig. 9.

Resistance R_{eq} consists of the capacitor ESR, transistors' $R_{\mathrm{ds,on}}$, and any other parasitic resistance in the charging path. In the following analysis, the charge sharing dynamics are assumed to be consistent with the SSL approximation, consistent with the prototype of Section VI. In the SSL, the impacts of R_{eq} are negligible [27], [31]. This approximation holds for the worst-case charging loop, when C_{x1} is connected to V_{load}, if

$$\max(\tau) = C_{xi} \left(2R_{\mathrm{ESR},C} + 4R_{\mathrm{ds,on}}\right) \ll \frac{T_s}{2}. \quad (14)$$

Because the switching frequency is a fixed $f_s = 150\,\mathrm{kHz}$, this inequality holds when the MSC is designed such that resistances are minimal and the capacitance C_{xi} is less than some maximum value. Increasing C_{xi} will reduce charge sharing losses until this inequality is violated, after which efficiency gains will be negligible due to the charge sharing dynamics approaching the fast switching limit (FSL) [27], [31].

In Fig. 7, if $\Delta v_{xx} = 0$, no loss occurs when the switch closes. However, with a voltage difference ($\Delta v_{xx} \neq 0$), the charge redistributes as the two capacitors are shorted. For capacitor C_{xx}, the voltage ripple is dictated by the portion of the power current i_{rec} going through the device

$$v_{xx} = \frac{1}{C_{xx}} \int_{t_x}^{t_{7-x}} |i_{\mathrm{rec}}| \sin(\omega t + \phi)dt + V_0 \quad (15)$$

where the initial voltage is equal to the output voltage, $V_0 = V_{\mathrm{load}}$, due to SSL operation. Solving the integral and ignoring the dc component give the voltage ripple on capacitor C_{xx}

$$\Delta v_{xx} = \frac{|i_{\mathrm{rec}}|}{\omega C_{xx}} \left(\cos(t_x\omega + \phi) - \cos(t_{7-x}\omega + \phi)\right). \quad (16)$$
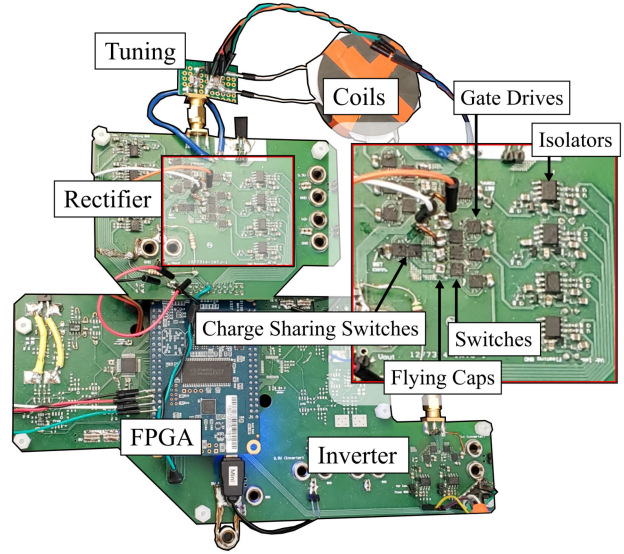
Assuming a small incremental voltage Δv_{xx}, a constant V_{load}, and $C_{\mathrm{load}} \gg C_{xx}$, then the charge sharing loss is

$$P_{\mathrm{cs}} = {}^1\!/_2\, C_{xx}\, \Delta v_{xx}^2\, f_s. \quad (17)$$

From (17), the charge sharing loss, which can be significant in hard-charging SC converters, is proportional to the switching frequency, capacitance, and voltage ripple on flying capacitors. Each of the flying capacitors, C_{x1} and C_{x2}, is subject to voltage ripple and consequent charge sharing loss defined in (17).

The conduction, charge sharing, and switching loss calculations each rely on approximations within the model. To test the accuracy of these approximations, the circuit model is compared with a prototype WPT system. Accurate prediction of the system-wide efficiency reinforces the validity of the modeling approach.

VI. EXPERIMENTAL RESULTS

The experimental setup is shown in Fig. 10. A single field-programmable gate array (FPGA) controls both a full-bridge inverter and the seven-level MSC rectifier, and both use the 30-V, 25-A half-bridge silicon module and gate driver listed in Table II. Floating voltages are required to drive each switch that is not grounded at its source. Many of these floating dc voltages are required for the seven-level SCC. Each floating voltage is generated via bootstrap circuitry, requiring no additional switching actions. Finally, the isolators seen in Fig. 10 are used to level-shift the FPGA pulsewidth modulation signals to the floating voltages.

The circuit used to provide floating supplies to each gate driver is shown in the partial schematic of Fig. 11. In the gray dashed boxes, commercial half-bridge drivers are used with bootstrap diode and decoupling capacitors for each gate driver. During the half-period where this phase leg is nonactive, all low side switches S_{xiL} and charge sharing switches S_{x4H} remain ON for

TABLE II
PROTOTYPE CHARACTERISTICS

Part / Characteristic	Part Number	Value
Silicon Module (HB)	BSZ0910NDXTMA1	—
Gate Driver (HB)	MP1907AGQ-P	—
Isolator	SI8423BB-D-IS	—
Controller	Altera Cyclone IV	—
Tx & Rx Coils	760308101141	10 μH
Switching Frequency	—	150 kHz
Input Voltage	—	7-20 V
Output Voltage	—	5.0 V
Rated Power	—	20 W

TABLE III
CIRCUIT VALUES OF EXPERIMENTAL PLATFORM

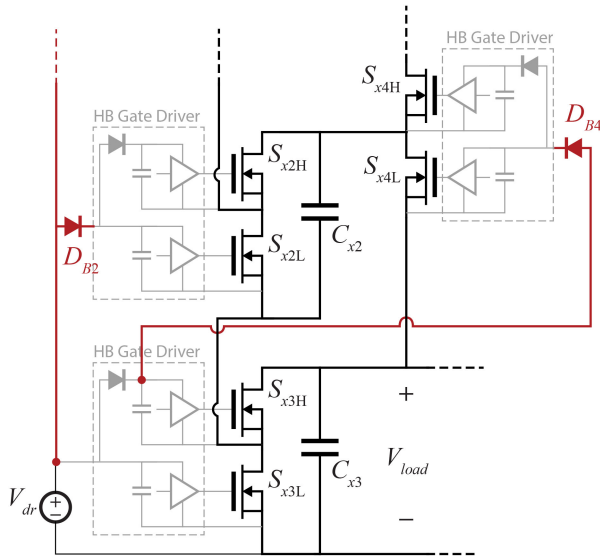| L_{tx}	C_p	R_p	C_{xx}
13.22 μH	757.56 nF	86.75 mΩ	15.66 μF
L_{rx}	C_s	R_s	C_{load}
13.26 μH	111.76 nF	118.48 $m\Omega$	27.41 μF
V_d	t_{on}	t_{off}	C_{oss}
0.78 V	1.4 ns	1.4 ns	525 pF
t_d	R_{dson}	$R_{ESR,C}$	k
13.33 ns	7.7 mΩ	1.39 $m\Omega$	0.773

Fig. 11. Bootstrapping scheme for gate drive power supplies.

duration $T_s/2$. During this time, D_{B2} will recharge the low-side supply of S_{x2L} from the gate drive supply voltage V_{dr}; the same will happen in the top module S_{x1L} and D_{B1} (not shown). For the charge sharing switches, D_{B4} recharges the supply of S_{x4L} whenever S_{x3H} is ON, which can be guaranteed by modulation pattern. Due to the use of silicon FETs with wide V_{gs} range, even with multiple diodes in the bootstrapping path, the reduced driving voltage does not significantly increase R_{dson}.

The wireless power tank is designed to reduce loss and compliment the study of the MSC rectifier. Two 9-A high-Q WPT coils are physically separated by thin paper dividers, fastened in place, and tuned. Either side of the tank is measured with the opposite side open, and a final measurement of the primary is taken with the secondary shorted. Values L_{tx}, L_{rx}, C_p, and C_s are reported by a Keysight E4990 A impedance analyzer. Capacitances C_p and C_s are composed of multiple discrete components in parallel, each of which is rated for 100 V. The coupling value of $k = 0.773$ is calculated by matching the theoretical circuit to the impedance analyzer measurements.

The impedance analyzer returns ESR values of 78.55 and 73.08 mΩ for the primary and secondary sides of the WPT

tank, setting the 150-kHz quality factors at 158.6 and 171.0, respectively. Next, blank rectifier and inverter printed circuit boards (PCBs) are semipopulated: The inverter has the input capacitance populated and one complimentary switching pair shorted, and the rectifier sees the switches in the ground path shorted ($v_{rec} = 0$). The ESR values of each PCB are measured at 150 kHz, and the final values of $R_p = (78.55 + 8.20)$ mΩ and $R_s = (73.08 + 45.40)$ mΩ are reported in Table III.

A 5-V dc bias derating is considered for the flying capacitance (C_{xx}). Four parallel 10-V, 0603 capacitors (C1608JB1A226M080AC) have measured total capacitance of 15.66 μF and 1.39 mΩ at 5-V bias, as shown in Table III. Because the flying capacitors are much larger than C_s and are only periodically inserted into the power path, the value of C_{xx} does not affect the WPT tank resonance.

Values V_d, C_{oss}, and R_{dson} are derived from the datasheet. $R_{ESR,C}$ is found by measuring a flying capacitor at 150 kHz. Times t_{on} and t_{off} are calculated using a gate drive current of 1 A and the Q_{gs} value from the device datasheet, and t_d is set as two clocks from the 150-MHz FPGA digital modulator.

With the component values defined in Table III, the worst-case charge redistribution is calculated to ensure that the system operates according to the SSL, i.e., the flying capacitors completely balance with V_{load} at each cycle. The minimal allotted time for charge redistribution is one half period, $T_s/2 = 1/(150\,\text{kHz}) \cdot 1/2 = 3.33$ μs. The worst-cast charge redistribution time constant is calculated by $\max(\tau) = (4R_{dson} + 2R_{ESR,C})C_{xx} = 0.53$ μs. Therefore, in the worst case, $3\tau_{wc}$ uses only 47% of the allotted time to achieve greater than 95% charge redistribution. Losses could be further reduced by increasing each flying capacitance C_{xx} until the FSL is reached, at the expense of greater board area.

The power stage shown in Fig. 12 is responsible for carrying the full power currents of the rectifier. The other circuitry that can be seen on the rectifier circuit board (upper PCB) in Fig. 10 is composed of dc voltage connectors, isolators, and digital control circuitry. Fig. 12 compares the rectifier power stage and a US quarter to convey the density of the layout. Without the need for bulky dc inductance, the rectifier is laid out to be a very small footprint. This compactness serves to reduce trace inductance and resistance, and it, therefore, also reduces consequent high frequency ringing and conduction loss. At $P_{out} = 20$ W, the power density of the MSC is 74.42 W/in^3. Notably, the only
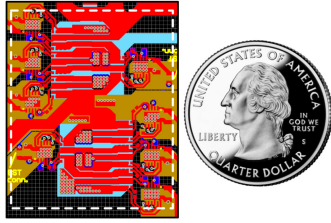
Fig. 12. PCB layout of the rectifier power stage (switches, power capacitors, gate drivers, and bootstrap circuitry) with a U.S. quarter for size reference. The white dotted line measures 31.4 mm × 27.5 mm.
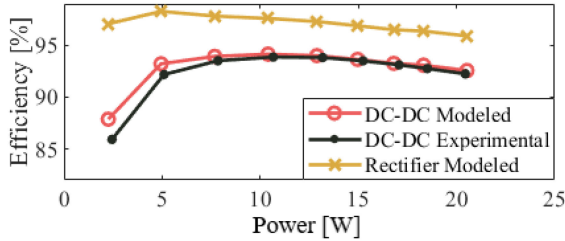

Fig. 13. DC–DC experimental data compared to the model for 2.45–20.45 W, including the modeled rectifier efficiency for reference.

Fig. 14. Experimental waveforms of the circuit at $P_{\text{out}} = 13.18$ W.

Fig. 15. Spectrum of the v_{rec} waveform in Fig. 14.

components on the bottom side of the board are bootstrap capacitors; so maneuvering only a few elements increases the power density to ≈ 103 W/in^3.

The seven-level SC rectifier enables output regulation without the need for a bulky filter inductance or discrete steps in voltage conversion. However, the layout in Fig. 12 only begins addressing the MSC's full potential to be a power dense topology. The experimental power density is limited by the use of discrete components; in the future, power stage integration onto a single IC, with only external capacitors, can substantially increase power density.

A. Experimental Data and Waveforms

Fig. 13 shows a comparison of the dc–dc experimental efficiency to the modeled dc–dc efficiency. Good agreement validates the modeling approach put forth in this article. The modeled rectifier efficiency is included and remains bounded between 95.9% and 98.3% for all surveyed points. One example test point is isolated from the nine experimental points in Fig. 13, and its waveforms are shown in Fig. 14. This point occurs at $P_{\text{out}} = 13.18$ W, demonstrates excellent efficiency, and maintains exceptionally low distortion. The two waveforms near the top of Fig. 14 are the rectifier input: v_{rec} and i_{rec}. The two bottom waveforms are the tank input (or inverter output): v_{inv} and i_{inv}.

The operating point is taken with a dc input voltage of 18.46 V and a dc output voltage of 5 V. The dc currents at the input of the inverter and the output of the rectifier are recorded. The oscilloscope waveform data shown in Fig. 14 is exported and processed in MATLAB. The fundamental voltage, current, and impedance of the rectifier are calculated for comparison with the model. This operating point occurs at $|Z_{\text{rec},1}| = 9.2\,\Omega$ and $\angle Z_{\text{rec},1} = 14.6°$. Matching this impedance to the model, the
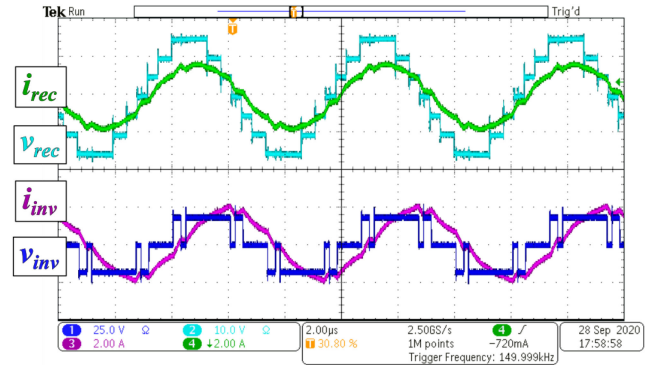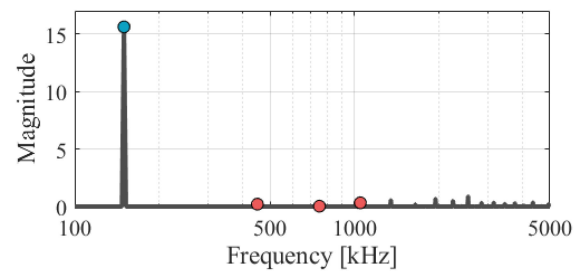
predicted output power and efficiency of 12.8 W and 93.5% are shown to be in good agreement with the experimental results of 13.2 W and 93.8%.

The waveform data are also evaluated for harmonic content. Fig. 15 shows the spectrum of waveform v_{rec} from Fig. 14. As predicted, the third, fifth, and seventh harmonics are significantly smaller than the fundamental component. Total waveform THD is calculated using

$$\text{THD}_i(x) = 100 \cdot \frac{\sqrt{\sum_{n=2}^{i} x_n^2}}{x_1} \quad (18)$$

where x_n is the rms value of the nth harmonic and x_1 is the rms value of the fundamental component. The THD$_7$ of v_{rec} in Fig. 14 is 2.44%.

In the experimental waveforms, the full-bridge inverter employs additional switching actions for further harmonic elimination. When harmonic content is reduced at both WPT voltages (v_{inv} and v_{rec}), the currents in the WPT tank are subject to significantly less distortion [30], [32]. The distortion considering only the first–seventh harmonics, THD$_7$, and the THD + noise, THD$_\infty$, values for each waveform in Fig. 14 are reported in Table IV. The distortion is quite low through the seventh harmonic, but higher frequency noise (including switching) contributes to a larger degree of distortion when including all harmonics, especially in the case of v_{inv}.
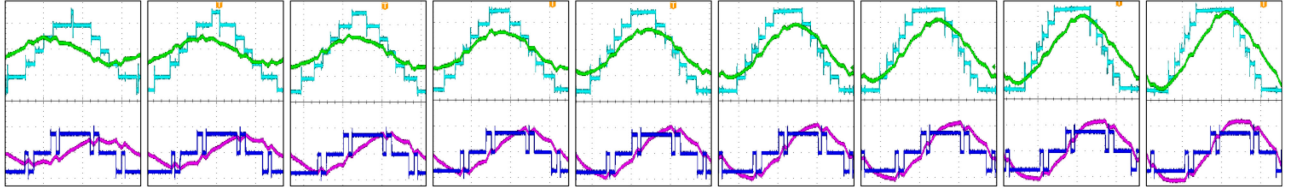
Fig. 16. Waveforms of experimental test points. Each image is a different experimental operating point with consistent oscilloscope scaling, laid out such that output power increases from left to right. The central image is repeated from Fig. 14.

TABLE IV
WAVEFORM DISTORTION IN FIG. 14

	1st	3rd	5th	7th	THD $_7$	THD $_\infty$
v_{rec} [V]	15.60	0.20	0.03	0.32	2.44	12.51
i_{rec} [A]	1.70	0.02	0.00	0.01	1.17	7.27
v_{inv} [V]	18.80	0.36	0.06	0.12	2.03	45.19
i_{inv} [A]	1.79	0.03	0.00	0.01	1.99	7.48

THD$_7$ and THD$_\infty$ of a square wave are 41.1% and 48.3%, respectively.
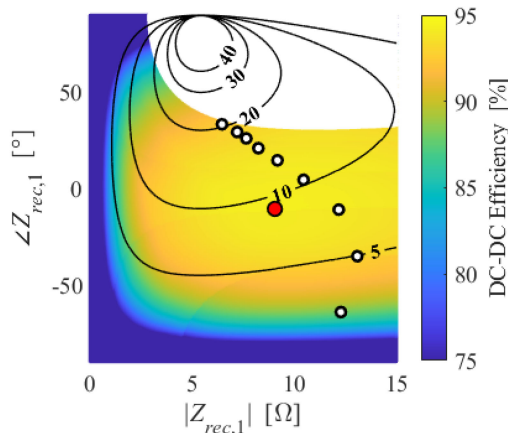

Fig. 17. Experimental data points overlaid on the complete loss model showing the efficiency (color gradient), power contours (black lines), and unreachable area (white) for $V_{load} = 5$ V.

B. Complete Experimental Power Sweep

Every experimental point is conducted without deviation from the parameters in Table III. Fig. 17 shows the total modeled system efficiency, output power, and reachable operating area. Output voltage $V_{load} = 5$ V remains constant, the modulation necessary to reach the white region ($M > 3.81$) is unattainable with the seven-level design, and the contour lines identify powers of up to 40 W. The experimental data points are overlaid on the modeled data for visualization of how the rectifier impedance is used to traverse the operating region. Each experimental point is composed of a different modulation index, control phase, and dc load, resulting in a range of output powers from 2.45 to 20.45 W.

This experimental trajectory through the operating space is near-optimal. The red dot indicates the peak system-wide efficiency, which is less than 0.5% higher than the nearest modeled test point.

The waveforms of each of these test points are summarized in order of ascending output power in Fig. 16. The modulation index increases with power, as does the phase at the input of the rectifier. To control the experimental test, the phase between v_{rec} and v_{inv} is varied, which can be seen clearly in Fig. 16. Note that Figs. 13, 16, 17, and 18 all refer to the same set of data points.

Fig. 18 gives details about the loss distributions, THD$_7$, and impedance of the experimental results. The modeled loss distribution in Fig. 18(a) shows that the tank and rectifier losses scale with power while the inverter losses remain nearly constant. The black line (and corresponding set of dots) is obtained by locating the point of minimal tank conduction loss for each power contour in Fig. 17, which results in the optimal loading trajectory per fundamental conduction losses. By comparing this line to the blue "Tank" bars, Fig. 18(a) illustrates how closely the experimental data set matches the optimal trajectory for tank efficiency. Because V_{in} is constant for the entire experimental dataset, the high-efficiency traversal from 2 to 20 W via controlling Z_{rec} does not require coordinated control with the inverter for power regulation.

The rectifier loss distribution in Fig. 18(b) is also model-based. The switching loss is a very small portion of the loss profile, and both the charge sharing and conduction losses are heavily influenced by increasing power.

Furthermore, a straightforward manipulation of (16) and (17) provides insight into how Fig. 18(b) changes with C_{xx} size. For a constant steady-state operating point, if $\sigma = |i_{rec}|/\omega \cdot (\cos(t_x \omega + \phi) - \cos(t_{7-x}\omega + \phi))$, then (17) is written as

$$P_{cs} = \sigma^2 / 2C_{xx} \tag{19}$$

showing that charge sharing loss is inversely proportional to the amount of flying capacitance. Take the highest power operating point in Fig. 18(b) as an example. The charge sharing loss is ≈ 400 mW for $C_{xx} = 15.66 \ \mu$F. If three of the four parallel capacitors used to implement C_{xx} were removed, the volume of each capacitor would reduce by 75%, but the charge sharing loss would increase to ≈ 1.6 W at $C_{xx} = 4 \ \mu$F.

Fig. 18(c) shows the experimental THD through the seventh harmonic for each waveform in the WPT tank. The waveforms remain at relatively low levels of distortion throughout the power sweep; the highest recorded THD remains below 13%. This
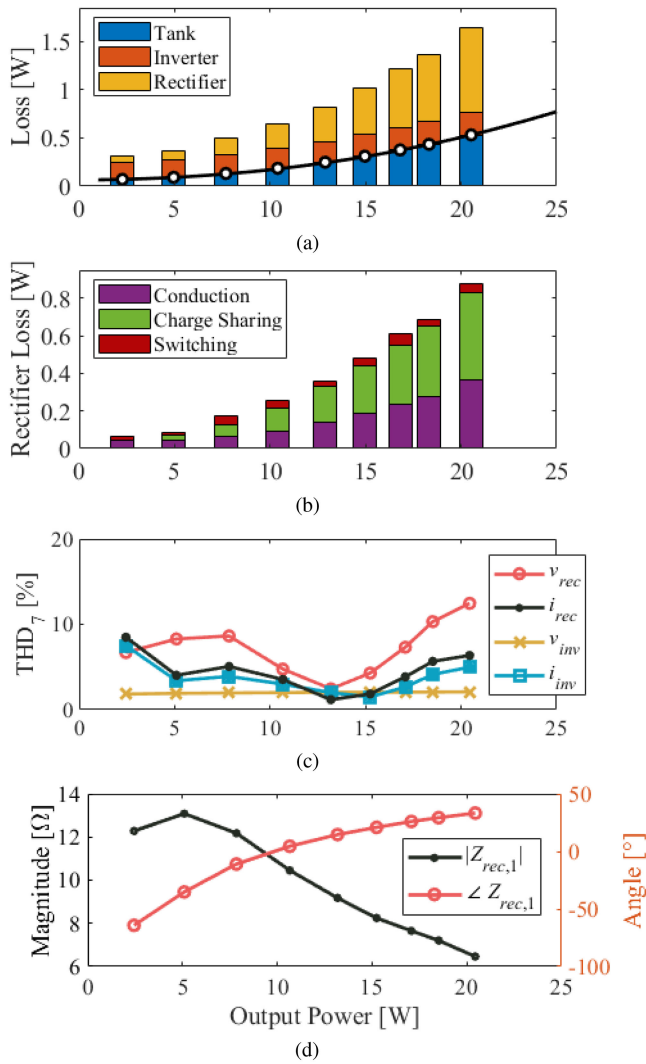
Fig. 18. Experimental results of (a) loss profile of the system, (b) loss profile of the rectifier, (c) harmonic distortion of all tank waveforms, and (d) fundamental impedance of the rectifier.

result is a significant improvement relative to the square waveforms in a traditional WPT system. The THD_7 of a square wave is 41.41%, but the THD_7 of v_{rec} is experimentally demonstrated to be much lower, bounded from 2.44% to 12.46%.

Fig. 18(d) shows the fundamental impedance (magnitude and phase) of the rectifier over the testing range. This plot characterizes the two axes of Fig. 17 and shows more clearly how the impedance of the rectifier can directly influence the power throughput of the system without significantly degrading system efficiency. In this set of test points alone, the MSC showcases low power operation and high power operation, consistently high efficiencies, resistive loading capability ($\angle Z_{\text{rec},1} \approx 0$), and dramatically reduced harmonic content. Each of these is achieved without externally adjusting the WPT coupling factor, tank tuning, inverter voltage, or fundamental operating frequency.

To demonstrate the MSC topology under different WPT tuning conditions, the primary and secondary side coils (originally tuned at 50 and 131 kHz) are retuned to 131 and 150 kHz, respectively. Other than the new values of C_p and C_s, the same
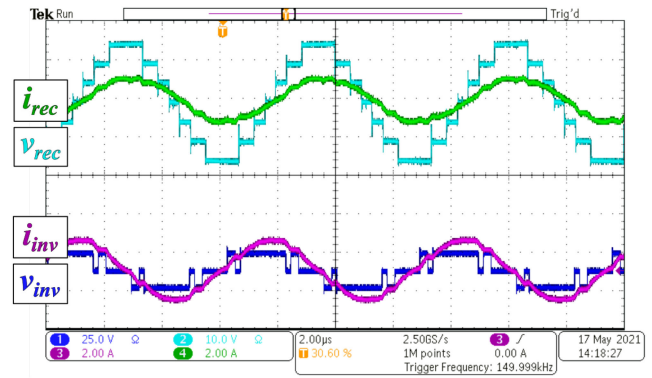

Fig. 19. Experimental waveforms of the retuned circuit at $P_{\text{out}} = 8.5$ W.

hardware is used, and the system is tested up to 19.86 W. Here, V_{in} is varied to compliment the desired output power. The MSC once again performs at a consistently high efficiency, with system-wide dc–dc measurements of 95.12% at 8.5 W and 92.95% at 19.85 W. Fig. 19 shows the waveforms of the 8.5-W operating point. The MSC topology is able to maintain a high efficiency under a wide range of WPT tank tuning and alignment scenarios.

Finally, Table V is included for comparison to other work with similar operating frequencies and output power levels. Table V includes THD values for holistic comparison. Measured values from prior literature are included whenever available and theoretical values are used otherwise; harmonic orders are reported in parentheses for measured results. Nevertheless, Table V presents the MSC in this article to be the only solution to simultaneously exhibit full step-up, step-down, and phase control while also demonstrating low THD without the need for bulky power inductors.

Two noteworthy challenges of MSC design are the number of switches and the amount of capacitance. Under the 5-V dc bias, the six flying capacitors have total capacitance of nearly 94 μF, and the number of switches is significantly higher than other approaches.

As with other multilevel converters, the total semiconductor area required is comparable to that of two-level implementations for the same power and input voltage v_{rec} due to the low voltage stresses on each individual device balancing the higher device count [8], [33]. surface mount device (SMD) capacitors maintain a low profile, very low ESR, and high power density relative to filter inductors [7], [8].

In Table V, the MSC topology exhibits superior performance in many metrics due to the ability to use the staircase waveform to simultaneously achieve multiple objectives, providing near-optimal system loading and high efficiency loading while simultaneously providing control and low harmonic content in a small footprint without bulky inductors. In alternative implementations, one-or-more aspect must be sacrificed. With full impedance control, the highest efficiency, and the lowest distortion, the topology showcases some significant advantage over each of the other approaches listed in Table V. Overall, the MSC approach manages highly efficient direct charging of a 5-V output without the need for an additional dc–dc converter.

TABLE V
COMPARISON TO OTHER PUBLISHED WPT RECTIFIERS

Reference	f_s	Rectifier	Control		k	P_{out}	V_{out}	η_{dc-dc}	THD$_i$ v_{rec} (i)	Rectifier Component Count		
			$|Z_{rec}|$	$\angle Z_{rec}$						Inductors	Switches	Capacitors
[11]	515 kHz	DHB + Boost dc-dc	↑	no	≈ 0.2	17.7 W	100 V	85%	≈ 48%^{2}	1 (dc-dc)	1+3D	2
[5]	200 kHz	Active Diff. Class E	↑	yes	0.71	24 W	12 V	90%	7.16% (10th)	2 (coupled)	2	1
[35]	200 kHz	Semi-active HB	↑	yes	–	16 W	24 V	–^{1}	46.3% (10th)	0	1+1D	1
[22]	205 kHz	AFB + Buck dc-dc	↑ / ↓	yes	0.6	11.2 W	4 V	77.3%	≈ 48%^{2}	1 (dc-dc)	6	2
[24]	100 kHz	Sync FB + LDO	↓	no	–	5.3 W	5.3 V	76%	≈ 48%^{2}	0	4	2
This Work	150 kHz	MSC	↑ / ↓	yes	0.77	20 W	5 V	93.8%^{3}	2.44%^{3} (7th)	0	16	7

^{1} No dc–dc efficiency given; rectifier ac–dc efficiency is ≈ 98%.
^{2} Theoretical value for squarewave, consistent with reporting in [5].
^{3} Values at P_{out} = 13.8 W.

VII. CONCLUSION

A seven-level switched capacitor rectifier is constructed in a 150-kHz WPT system. The rectifier is compact, efficient, real-time tunable, and capable of reducing waveform distortion. An FHA circuit model is constructed to include conduction, switching, and charge sharing losses. The inverter and rectifier are both experimentally switched to reduce waveform harmonic content.

The experimental data points are laid over the model in terms of Z_{rec} to convey how the rectifier's tuning capabilities enable traversal of the WPT operating region. The modeled dc–dc efficiency is shown to be in good agreement with the experimental data, and the modeled rectifier efficiency is between 95.9% and 98.3% for all tested power levels. THD is also low across the full power sweep, validating the MSC as a strong candidate for highly efficient, compact rectification in consumer device WPT applications.

REFERENCES

[1] C. Zhao, D. Costinett, and S. Yang, "A seven-level switched capacitor AC-DC rectifier for fast wireless charging," in *Proc. IEEE PELS Workshop Emerg. Technol.: Wireless Power Transf.*, 2018, pp. 1–6.
[2] "Qualcommquick charge 5," qualcomm.com. Accessed: Jan. 23, 2022. [Online]. Available: https://www.qualcomm.com/products/features/quick-charge
[3] "Wireless power consortium," wirelesspowerconsortium.com. Accessed: Jan. 23, 2022. [Online]. Available: https://www.wirelesspowerconsortium.com/
[4] J. Wu, C. Zhao, Z. Lin, J. Du, Y. Hu, and X. He, "Wireless power and data transfer via a common inductive link using frequency division multiplexing," *IEEE Trans. Ind. Electron.*, vol. 62, no. 12, pp. 7810–7820, Dec. 2015.
[5] K. Li, S. C. Tan, and R. S. Y. Hui, "Single-stage regulated resonant WPT receiver with low input harmonic distortion," *IEEE Trans. Power Electron.*, vol. 35, no. 7, pp. 6820–6829, Jul. 2020.
[6] W. X. Zhong and S. Y. R. Hui, "Maximum energy efficiency tracking for wireless power transfer systems," *IEEE Trans. Power Electron.*, vol. 30, no. 7, pp. 4025–4034, Jul. 2015.
[7] P. A. Kyaw, A. L. F. Stein, and C. R. Sullivan, "Fundamental examination of multiple potential passive component technologies for future power electronics," *IEEE Trans. Power Electron.*, vol. 33, no. 12, pp. 10708–10722, Dec. 2018.
[8] S. R. Sanders, E. Alon, H.-P. Le, M. D. Seeman, M. John, and V. W. Ng, "The road to fully integrated DC–DC conversion via the switched-capacitor approach," *IEEE Trans. Power Electron.*, vol. 28, no. 9, pp. 4146–4155, Sep. 2013.
[9] D. Ahn, S. Kim, S. Kim, J. Moon, and I. Cho, "Wireless power transmitter and receiver supporting 200-kHz and 6.78-MHz dual-band operation without magnetic field canceling," *IEEE Trans. Power Electron.*, vol. 32, no. 9, pp. 7068–7082, Sep. 2017.

[10] A. Satyamoorthy *et al.*, "Wireless power receiver for mobile devices supporting inductive and resonant operating modes," in *Proc. IEEE Wireless Power Transf. Conf.*, 2014, pp. 52–55.
[11] H. Li, J. Li, K. Wang, W. Chen, and X. Yang, "A maximum efficiency point tracking control scheme for wireless power transfer systems using magnetic resonant coupling," *IEEE Trans. Power Electron.*, vol. 30, no. 7, pp. 3998–4008, Jul. 2015.
[12] M. Fu, H. Yin, X. Zhu, and C. Ma, "Analysis and tracking of optimal load in wireless power transfer systems," *IEEE Trans. Power Electron.*, vol. 30, no. 7, pp. 3952–3963, Jul. 2015.
[13] Y. Yang, W. Zhong, S. Kiratipongvoot, S. Tan, and S. Y. R. Hui, "Dynamic improvement of series–series compensated wireless power transfer systems using discrete sliding mode control," *IEEE Trans. Power Electron.*, vol. 33, no. 7, pp. 6351–6360, Jul. 2018.
[14] Z. Huang, S. Wong, and C. K. Tse, "Control design for optimizing efficiency in inductive power transfer systems," *IEEE Trans. Power Electron.*, vol. 33, no. 5, pp. 4523–4534, May 2018.
[15] M. D. Seeman and S. R. Sanders, "Analysis and optimization of switched-capacitor DC–DC converters," *IEEE Trans. Power Electron.*, vol. 23, no. 2, pp. 841–851, Mar. 2008.
[16] B. Wu, L. Wang, L. Yang, K. M. Smedley, and S. Singer, "Comparative analysis of steady-state models for a switched capacitor converter," *IEEE Trans. Power Electron.*, vol. 32, no. 2, pp. 1186–1197, Feb. 2017.
[17] M. D. Seeman, V. W. Ng, H. Le, M. John, E. Alon, and S. R. Sanders, "A comparative analysis of switched-capacitor and inductor-based DC-DC conversion technologies," in *Proc. IEEE 12th Workshop Control Model. Power Electron.*, 2010, pp. 1–7.
[18] Y.-J. Park *et al.*, "A design of inductive coupling wireless power receiver with high efficiency active rectifier and multi feedback LDO regulator," in *Proc. IEEE Wireless Power Transf. Conf.*, 2016, pp. 1–4.
[19] B. Jang, S. Oh, Y. Park, and K. Y. Lee, "A high efficiency active rectifier with zero current sensing for loosely-coupled wireless power transfer systems," in *Proc. IEEE Int. Conf. Consum. Electron.-Asia*, 2016, pp. 1–2.
[20] D. Huwig and P. Wambsganß, "Digitally controlled synchronous bridge-rectifier for wireless power receivers," in *Proc. 28th Annu. IEEE Appl. Power Electron. Conf. Expo.*, Mar. 2013, pp. 2598–2603.
[21] R. Gallichan, D. M. Budgett, and D. McCormick, "600 mW active rectifier with shorting-control for wirelessly powered medical implants," in *Proc. IEEE Biomed. Circuits Syst. Conf.*, 2018, pp. 1–4.
[22] A. Berger, M. Agostinelli, S. Vesti, J. A. Oliver, J. A. Cobos, and M. Huemer, "A wireless charging system applying phase-shift and amplitude control to maximize efficiency and extractable power," *IEEE Trans. Power Electron.*, vol. 30, no. 11, pp. 6338–6348, Nov. 2015.
[23] S. Cochran and D. Costinett, "Frequency synchronization and control for a 6.78 MHz WPT active rectifier," in *Proc. IEEE 19th Workshop Control Model. Power Electron.*, Jun. 2018, pp. 1–7.
[24] Integrated Device Technology, "Qi wireless power receiver with integrated rectifier and LDO output," *P9025AC datasheet*, Sep. 2015.
[25] W. Li and D. J. Perreault, "Switched-capacitor step-down rectifier for low-voltage power conversion," in *Proc. 28th Annu. IEEE Appl. Power Electron. Conf. Expo.*, 2013, pp. 1884–1891.
[26] Würth Elektronik, "WE-WPCC wireless power transfer transmitter coil," *760308101141 datasheet*, Jul. 2017.
[27] M. S. Makowski and D. Maksimovic, "Performance limits of switched-capacitor DC-DC converters," in *Proc. PESC - Power Electron. Specialist Conf.*, vol. 2, 1995, pp. 1215–1221.

[28] L. M. Tolbert and T. G. Habetler, "Novel multilevel inverter carrier-based PWM method," *IEEE Trans. Ind. Appl.*, vol. 35, no. 5, pp. 1098–1107, Sep./Oct. 1999.

[29] L. M. Tolbert, Z. F.Peng, and T. G. Habetler, "Multilevel converters for large electric drives," *IEEE Trans. Ind. Appl.*, vol. 35, no. 1, pp. 36–44, Jan./Feb. 1999.

[30] C. Zhao and D. Costinett, "GaN-based dual-mode wireless power transfer using multifrequency programmed pulse width modulation," *IEEE Trans. Ind. Electron.*, vol. 64, no. 11, pp. 9165–9176, Nov. 2017.

[31] M. Seeman, "A design methodology for switched-capacitor dc-dc converters," Ph.D. dissertation, Univ. California Berkeley, Berkeley, CA, USA, 2009.

[32] C. Zhao, S. Cochran, D. Costinett, and S. Yang, "Design and evaluation of a multilevel switched capacitor rectifier for wireless fast charging," in *Proc. IEEE Appl. Power Electron. Conf. Expo.*, 2019, pp. 833–840.

[33] J. T. Stauth, "Pathways to mm-scale DC-DC converters: Trends, opportunities, and limitations," in *Proc. IEEE Custom Integr. Circuits Conf.*, 2018, pp. 1–8.

[34] K. Li, A. T. L. Lee, S.-C. Tan, and R. S. Y. Hui, "Highly efficient single-switch-regulated resonant wireless power receiver with hybrid modulation," *IEEE Trans. Emerg. Sel. Topics Power Electron.*, vol. 9, no. 3, pp. 3770–3780, Jun. 2021.

Chongwen Zhao (Member, IEEE) received the B.Sc. degree from the School of Electronic Engineering, Xidian University, Xi'an, China, in 2011, the M.Sc. degree from the College of Electrical Engineering, Zhejiang University, Hangzhou, China, in 2014, and the Ph.D. degree in electrical engineering from the University of Tennessee, Knoxville, TN, USA, in 2018.

He is currently a Senior Hardware Engineer with Apple, Cupertino, CA, USA, and serves as a Tech Lead for wireless charging of wearable products. His research interests include wireless power system design, high power-density converter design, and silicon system integration.

Dr. Zhao was the recipient of Second Prize Paper at IEEE PELS Workshop on Emerging Technologies: Wireless Power in 2018.

Spencer Cochran (Member, IEEE) was born in Knoxville, TN, USA, in 1992. He received the B.Sc. degree in electrical engineering in 2015, the M.Sc. degree in 2017, and the Ph.D. degree in 2021, all from the University of Tennessee, Knoxville, TN, USA.

His graduate work focused on wireless power transfer at both 150 and 6.78 MHz, which included power stage design, system tuning, distortion reduction, and dual-loop control design. He was a Robert E. Bodenheimer Fellow during his master's work and a Tennessee Fellow for Graduate Excellence during his tenure as a doctoral student. He is currently a Power Engineer with Astranis Space Technologies Corp., San Francisco, CA, USA, where he aids in power electronics designs for their satellite systems. His research interests include high switching frequency converter design, wireless power transfer, and control modeling.

Dr. Cochran, while at the University of Tennessee, completed the Wide Bandgap Traineeship and received an award for exemplary research in 2020.

Daniel Costinett (Senior Member, IEEE) received the Ph.D. degree in electrical engineering from the University of Colorado Boulder, Boulder, CO, USA, in 2013.

He is currently an Associate Professor with the Department of Electrical Engineering and Computer Science, University of Tennessee, Knoxville (UTK), TN, USA. He is currently the Codirector of Education and Diversity with the National Science Foundation/Department of Energy Engineering Research Center for Ultra-Wide-Area Resilient Electric Energy Transmission Networks (CURENT). His research interests include resonant and soft switching power converter design, high efficiency wired and wireless power supplies, ON-chip power conversion, medical devices, and electric vehicles.

Dr. Costinett was a recipient of the National Science Foundation CAREER Award in 2017, the 2016 and 2020 IEEE PELS Transactions Second Place Prize Paper Award, and the 2015 IEEE IAS William M. Portnoy Award. He currently serves as an Associate Editor for the IEEE JOURNAL OF EMERGING AND SELECTED TOPICS IN POWER ELECTRONICS and IEEE TRANSACTIONS ON POWER ELECTRONICS.